Interfacial Microstructure Evolution due to Strain Path Changes in Sliding Contacts

Stefan J. Eder,*,†,‡ Ulrike Cihak-Bayr,† Carsten Gachot,†,‡ and Manel Rodríguez Ripoll†

†*AC2T research GmbH, Viktor-Kaplan-Straße 2/C, 2700 Wiener Neustadt, Austria*

‡*Institute for Engineering Design and Logistics Engineering, Vienna University of Technology, Getreidemarkt 9, 1060 Vienna, Austria*

E-mail: stefan.eder@ac2t.at

Phone: +43 (0)2622 81600 161. Fax: +43 (0)2622 81600 99

Abstract

We performed large-scale molecular dynamics (MD) simulations to study the transient softening stage that has been observed experimentally in sliding interfaces subject to strain path changes. The occurrence of this effect can be of crucial importance for the energy efficiency and wear resistance of systems that experience changes in sliding direction, such as bearings or gears in wind parks, piston rings in combustion engines, or wheel–rail contacts for portal cranes. We therefore modeled the sliding of a rough counterbody against two polycrystalline substrates of fcc copper and bcc iron with initial near-surface grain sizes of 40 nm. The microstructural development of these substrates was monitored and quantified as a function of time, depth, and applied pressure during unidirectional sliding for 7 ns. The results were then compared to the case of sliding in one direction for 5 ns and reversing the sliding direction for an additional 2 ns. We observed the generation of partial dislocations, grain refinement and rotation, as well as twinning (for fcc) in the near-surface region. All microstructures were increasingly affected by these processes when maintaining the sliding direction,

but recovered to a great extent upon sliding reversal up to applied pressures of 0.4 GPa in the case of fcc Cu and 1.5 GPa for bcc Fe. We discuss the applicability and limits of our polycrystalline MD model for reproducing well-known bulk phenomena such as the Bauschinger effect in interfacial processes.

Keywords: microstructure evolution; strain path change; Bauschinger effect; molecular dynamics

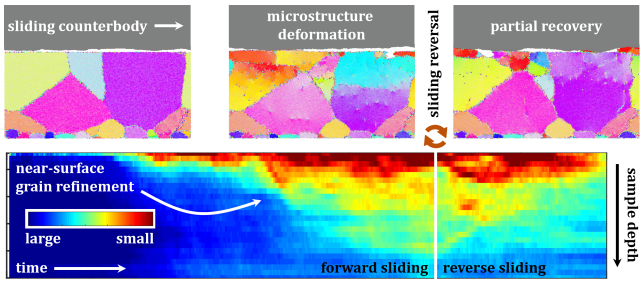

1 Introduction

Metallic machine elements that operate under sliding conditions can be found in many daily life applications. These applications are diverse and range from bearings, combustion engine elements, and other automotive components to wheels in trains or in industrial cranes. A detailed understanding of their surface degradation mechanisms that ultimately lead to failure is essential for insuring their safe operation. In this context, a significant research effort spanning the past 40 years aims to understand the interfacial microstructure evolution of metals during sliding contact.[1–3]

Sliding of metallic surfaces is a complex process, since it involves high strains that may lead to severe plastic deformation, large strain gradients, high strain rates and strain rate gradients, intermixing of materials, as well as microstructural recovery and recrystallization.[4,5] The imparted severe plastic interfacial deformation during sliding results in the generation of dislocations as soon as the stress state in the activated volume reaches the yield stress criterion, which can be well below the macroscopic yield stress of the bulk. The arrangement of the generated dislocations can proceed as small angle grain boundaries, ultimately leading to grain refinement and the presence of a well-defined nanocrystalline layer in the immediate vicinity of the metal interface.[1–3] According to recent experimental evidence, the origin of the sharp discontinuity between the sub-surface nanocrystalline zone and the coarse-grained substrate underneath seems to lie in the formation of a dislocation trace line parallel to the surface[6] in the very early stages of interfacial microstructure evolution. On the contrary, it was experimentally observed more recently that sliding on initially ultrafine-grained metallic surfaces can lead to recrystallization and grain coarsening.[7,8] The regimes and conditions that determine grain refinement and grain coarsening were recently studied for face-centered cubic (fcc) metals in 9 with emphasis on their impact on friction. Molecular dynamics (MD) studies of interfacial deformation mechanisms in nanocrystalline metals have shown that for grains smaller than 30 nm in diameter, plasticity is dominated by grain boundary sliding, whereas larger grains deform mostly by dislocation motion and eventually twinning,[10] de-

pending on their crystallographic structure, strain rate, and stacking fault energy.

The study of microstructure evolution beneath the contact interface in sliding systems has focused almost exclusively on the deformation imparted by a unidirectionally sliding counterbody.[1–3,11,12] Alternatively, some works addressed microstructure evolution under reciprocating sliding conditions, as for example 6,13. However, one crucial aspect has received very little attention so far. What happens in the microstructure of a metal at the moment when the sliding direction is reversed? This question is not only of scientific interest, but also relevant for a large number of technological systems, because industrial components are frequently faced with sliding reversals, e.g., bearings or train wheels. This situation differs from reciprocating sliding in the sense that the bearings operate in a preferred direction of sliding/rotation. This preferred direction is typically maintained until a given interfacial microstructure is well-established, typically severely plastically deformed and afterwards the sliding direction may be reversed under a given set of operating conditions. This situation is distinct from a linearly reciprocating system, where a component oscillates around an intermediate position so that both sliding directions occur equally at a given frequency, such as a piston ring in a combustion engine. A key factor for understanding surface degradation that ultimately leads to wear and component failure is a clear picture of microstructure evolution near the interface of sliding counterparts.

It is well established that a reversal of the strain direction in metallic bulk materials leads to an offset of the yield stress. The reason for this is attributed to internal back-stresses generated before reversing the strain direction. The back-stresses induced during monotonic loading aid the activation of dislocation glide in the reverse direction, so that the flow stress is initially lower immediately after the strain path change when compared to the monotonic stress behavior. This effect is called Bauschinger effect,[14] named after the eponymous professor who described it for the first time in 1886.[15] In metals pre-deformed by severe plastic deformation, a reversal in the strain direction leads to such dramatic microstructural changes that the offset of the yield stress is often accompanied by a stagnation of the flow stress evolution or even a transient softening stage depending on the severity of the imparted pre-deformation.[16] After this transient stage, the material recovers its strain hardening behavior when continuing the deformation along the new strain path. A transient change in the flow stress evolution upon strain path changes has been reported for many metals such as aluminum alloys,[17,18] copper,[19,20] steels,[21–24] zircaloy,[25] beryllium,[26,27] and tungsten.[28] All these metals were deformed under several strain path changes, such as tension-compression, reversal of shear direction, and pre-deformation by equal-channel angular extrusion or wire drawing. Strain reversals also play a crucial role in rolling processes.[14] The change in flow stress evolution occurs because the dislocation structure formed during monotonic loading is gradually replaced by the structure generated in the new strain path.[29,30] Dislocation structures formed during pre-loading, such as sub-cells, are dissolved after reversing the loading direction.

Many systems in technological applications experience such conditions, e.g., a steering wheel bearing during parking, bearings and tooth gears in wind parks, or train wheels when operating on a single track. The impact of reversing the sliding direction has only been addressed in a handful of papers. The reason for the lack of systematic research of sliding reversals probably lies in the way that tribological experiments are typically performed, i.e., either under unidirectional or reciprocating sliding contact conditions. Pio-

neering attempts, aimed at investigating the role of strain reversal in sliding contacts on microstructure evolution and wear resistance, focused on experiments going in one direction for a defined number of cycles and back for the same number of cycles.[31–34] However, properly designed strain reversal experiments require a large degree of plastic deformation imparted in strain direction before analyzing the microstructural evolution during the transient stage, immediately after reversing strain. Consequently, a better analogy with strain reversal experiments on bulk materials was recently proposed by Rodríguez Ripoll *et al.*[35] Their methodology relies on performing unidirectional experiments until reaching a fixed degree of plastic deformation and subsequently reversing the sliding direction only for a lower number of cycles. By this means, the transient softening stage can be clearly identified.

As experimental tests for of the Bauschinger effect in sliding contacts are rather tedious and complex, the aim of this work is to model strain path effects in a sliding interface using large-scale polycrystalline MD simulations. Polycrystalline MD simulation has proven to be a powerful tool for providing detailed insight into the microstructural evolution of materials close to the surface.[36] Eder *et al.*[37] have shown that polycrystalline MD models of ferrite can account for grain growth at the surface and grain orientation changes. In contrast to macro- or mesoscopic modeling approaches, MD explicitly considers the crystallographic aspects of the involved solids down to the dislocation level without the necessity of constitutive material models. With the steady increase of computational power, manageable system sizes have now grown to tens of millions of atoms, which translates into grain sizes that can reproduce macroscopic plasticity behavior, i.e., no grain boundary sliding, but dislocation pile-up and grain refinement. Our study focuses on copper and body-centered cubic (bcc) iron surfaces, since these two cubic lattices and these metals are the basis for typical commercial alloys and cover technologically relevant applications. Furthermore, their example will serve to study the strain path change behavior in sliding contacts in metals with face-centered and body-centered cubic crystal structures.

2 Methods

All our simulations were carried out using the open-source MD code LAMMPS.[38] The polycrystalline MD model, see Fig. 1, was constructed using two separate 3D-periodic Voronoi tessellations, one for the large surface grains with an effective grain diameter of 38.9 nm and one for the small base grains (9.6 nm) that only serve as a layer for applying the boundary conditions, i.e., keeping the lowest 3 Å of the sample rigid without preventing grain rotation, etc., at the surface. These two regions were then joined by an interface with an RMS roughness of 1.5 nm to prevent the formation of an artificial sliding interface between the two, leading to the final polycrystalline sample dimensions of $85 \times 85 \times 40$ nm^3, or approximately 25 million atoms. The sample surface was kept atomically flat. The fcc Cu sample was heat treated at 650 K for 240 ps, after which it was quenched within 20 ps to 300 K. The heat treatment temperature for the bcc Fe sample with the same grain structure and orientation was 1100 K. More information on the generation of the polycrystalline structure can be found in 36. For an overview of the system assembly and how the heat treatment effects the recrystallization of the interfacial region, see Fig. 1.

The rigid counterbody was constructed as a bcc (100) Fe monocrystal with an RMS surface roughness of 0.5 nm, a fractal dimen-

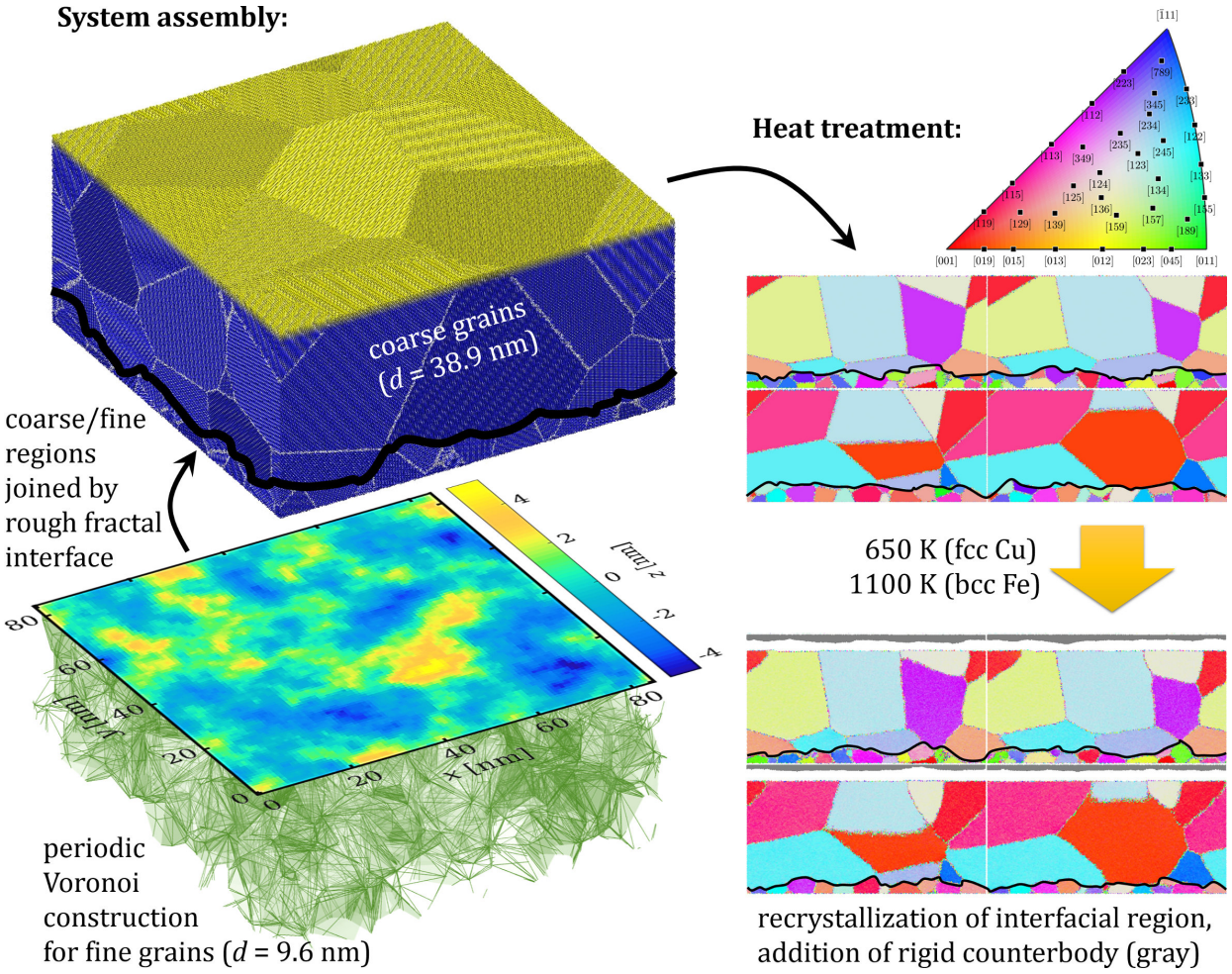

Figure 1: Assembly of the 3D molecular dynamics model. Left side: illustration of how the coarse and the fine grains are joined by means of a rough fractal interface (heat map / thick black lines). Right side: illustration of how the heat treatment leads to the disappearance of truncated fine grains via recrystallization (images are exemplary slices parallel to the xz plane, colors denote grain orientation, see legend).

sion of 2.186, and a typical lateral roughness feature extent of 33 nm, where the lattice constant was stretched by 0.23 % to ensure clean periodic boundary conditions along the lateral system dimensions. Interactions within the fcc Cu sample are controlled by an EAM potential from 39, those within the bcc Fe sample by a Finnis-Sinclair potential[40] from 41. Both are widely used force fields for their respective materials and have been repeatedly applied to tribological problems featuring sliding or abrasive systems.[42–44] For the interactions between the counterbody and the sample, Lennard-Jones potentials were adapted to imply a third body, so that the results reflect a typical sliding process that explicitly considers friction, rather than a sheared interface between two pure metal surfaces in ultra-high vacuum.[45] This led to parameters of $\sigma_{\mathrm{Fe}} = 0.2203$ nm, $\sigma_{\mathrm{Cu}} = 0.224$ nm, and $\varepsilon = 0.095$ eV, the latter obtained from a parameter study in which the system response to the variation of the depth of the potential well was analyzed. As a simplification, no explicit (boundary) lubricant was included in our MD model, as the observed effects were expected to be more pronounced under dry friction.

The counterbody was moved across the surface of the sample at a sliding velocity in x direction of $v^{(\mathrm{slide})} = 80$ m/s (chosen for computational feasibility) and an angle of 6.42° with the x-axis, so that roughness features re-enter the simulation box at different y positions every time they pass the periodic box boundaries and therefore never follow exactly in their own paths, which reduces artifacts associated with the small system size. The normal pressure σ_z on the substrate (defined as the total force in $-z$ direction acting on it divided by the lateral cross-section of the simulation box, 7225 nm^2) was kept constant at values ranging from 0.1 to 0.5 GPa (0.6 to 1.8 GPa for Fe) for an initial simulation time of 5 ns. In order to explore the effects of sliding direction reversal on the microstructure of the samples, two more simulation runs of 2 ns each were performed for every normal pressure, starting from the endpoint of the initial simulations, one in the original sliding direction and one in the opposing one.

Removal of frictional heat from the sample was performed using a Langevin thermostat acting on all the non-rigid sample atoms, effectively implementing an electron-phonon coupling scheme with the electrons acting as an implicit heat bath. The coupling times between the atoms and the thermostat were adjusted to reflect the macroscopic thermal conductivity of the respective material (0.5 ps for Cu, 3.5 ps for Fe), ensuring realistic temperature gradients.[37] The thermostat acts only in y direction, (nearly) perpendicular to the directions of normal pressure and sliding, so as not to overly interfere with these external constraints.

The visualizations of the sample microstructures are tomographic sections colored according to grain orientation as in electron backscatter diffraction, using the inverse pole figure coloring standard. The orientations were calculated using polyhedral template matching[46] as implemented in OVITO,[47] and the color rendition was carried out using the MTEX toolbox[48,49] for Matlab.

Quantification of grain refinement was carried out via a common neighbor analysis (CNA)[50,51] with a neighborhood cutoff radius of 0.3086 nm for fcc Cu and 0.3446 nm for bcc Fe. The CNA determines the local crystal structure around each atom by calculating a pattern that depends on the nearest neighbors of that atom. It differentiates between fcc, hcp, bcc, icosahedral, and unknown patterns. The twin boundaries in the fcc structure of Cu are unambiguously identified as hcp, while grain boundaries, dislocations, and surfaces (as well as regions amorphized by severe deformation) are all identified as "unknown". Using only CNA, it is

therefore not possible to distinguish between the three different types of "unknown" atoms listed above. With this in mind, however, it still remains a useful means of quantification for phenomena such as grain refinement, even if a pronounced shear zone forms in the top layers of the samples, characterized by atomic drift velocities of several m/s (the evaluation of which is discussed in more detail in 52). Histograms of the grain boundary and twin boundary (for fcc) atoms along the z direction of the samples with a bin width of 1 nm were calculated at every time step to yield a time-dependent depth profile of the grain boundary and dislocation fraction as well as the twin boundary fraction for fcc. These depth profiles were then visualized as heat maps, where the color denotes the percentage of grain or twin boundaries in that depth layer at that time. For presentation purposes, data for $z < 15$ nm was omitted in these maps, as they are dominated by the fine-grained boundary layer, which might distract from the microstructural developments in the near-surface region. The nonlinear relationship between the grain boundary fraction and the grain diameter in (nano)crystalline copper, shown in the insert in Fig. 4, was adapted from 10 by adding data points from our own Cu system and performing a rational-function fit to the data so that a typical grain diameter d in nm may be calculated for a given grain boundary fraction ρ (in %) via $d = 226\,\rho^{-1.08}$. Using this relationship, it is possible to directly visualize the time development of grain refinement or coarsening, provided that dislocations do not dominate the fraction of atoms identified as grain boundaries, which is reasonably the case for fcc Cu, but not for bcc Fe.

3 Results

3.1 Microstructure evolution of an fcc Cu polycrystal

Representative snapshots of a sliding simulation of a rigid slider against fcc Cu are shown in Fig. 2 and comprise the initial 5 ns unidirectional sliding followed by additional 2 ns sliding, either in the same initial direction or in the reverse direction. The initial microstructure is set-up by equiaxed, defect-free grains, see Fig. 2a. After 3 ns, the initial microstructure becomes deformed as a consequence of dislocation generation and glide as well as twin formation, accompanied by intragranular rotation (Fig. 2c). The severity and depth affected by the imparted deformation depends on the applied normal load. In the presented example, dislocation activity is restricted to approximately half of the substrate depth. With increasing sliding time (5 ns), the formed sub-grains begin to consolidate, and partial grain rotation can be observed within the large grains as graded hues, which represent stored intragranular elastic strains. Grain refinement occurs up to a depth of 15 nm.

At this point, if we follow the sliding direction for two additional ns, dislocation activity reaches the bottom of the substrate and the bottom grains start changing their crystallographic orientation, e.g., the large red grain originally oriented in [100] has rotated to [012] (yellow) in Fig. 2f. Between these rotated grains and the surface, evident signs of severe plastic deformation are visible as indicated by the presence of a large number of lattice defects. By contrast, if we reverse the sliding direction (Fig. 2e), we observe that the microstructure undergoes a partial recovery that qualitatively resembles much more the microstructure obtained after 3 ns than the equivalent microstructure obtained after 7 ns. This dissolution of

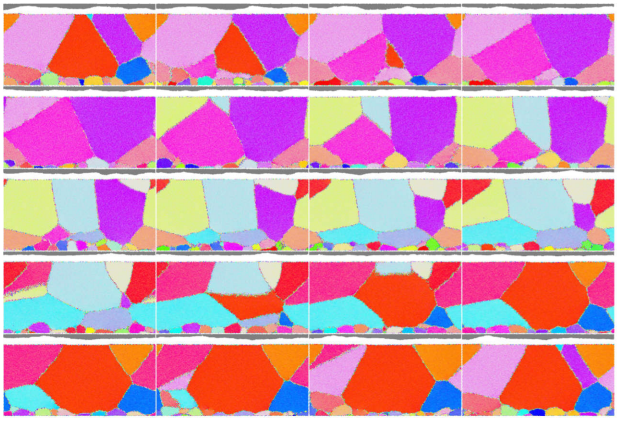

(a) $t = 0$ ns

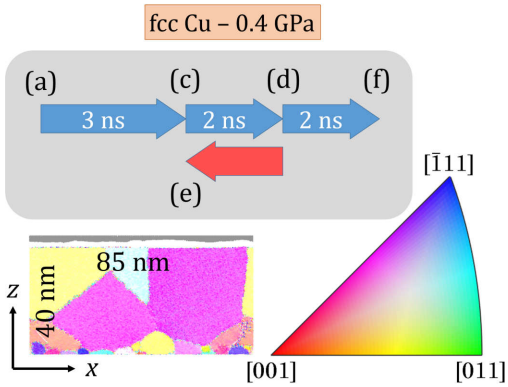

(b)

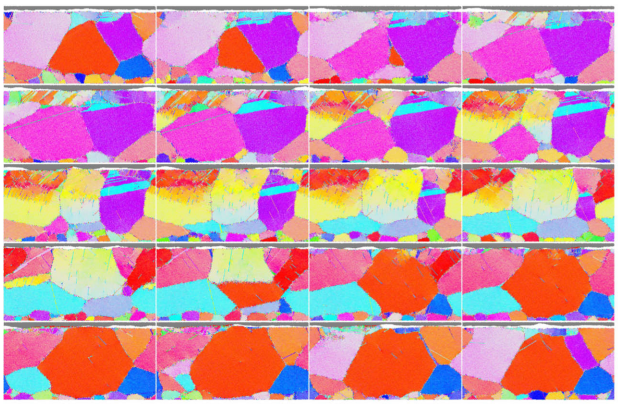

(c) $t = 3$ ns

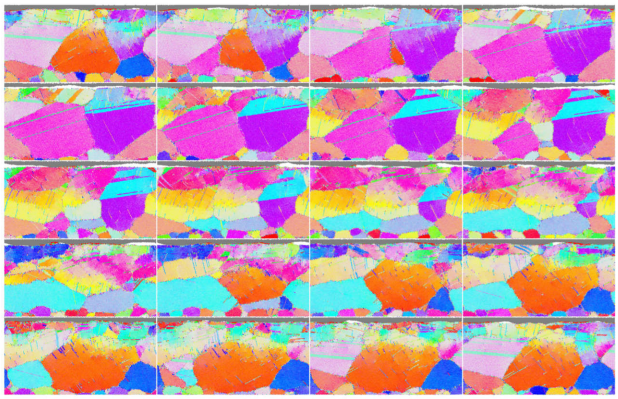

(d) $t = 5$ ns (turning point)

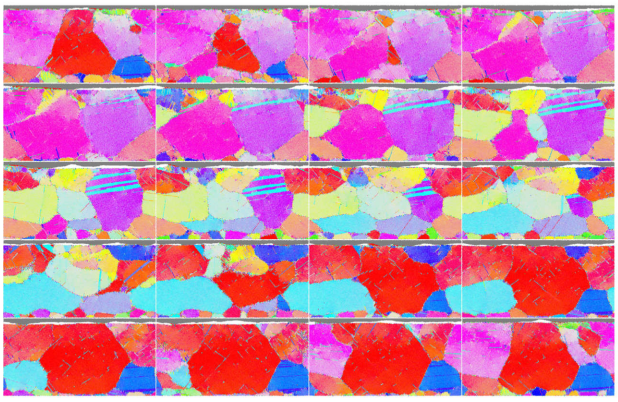

(e) $t = 7$ ns (reverse)

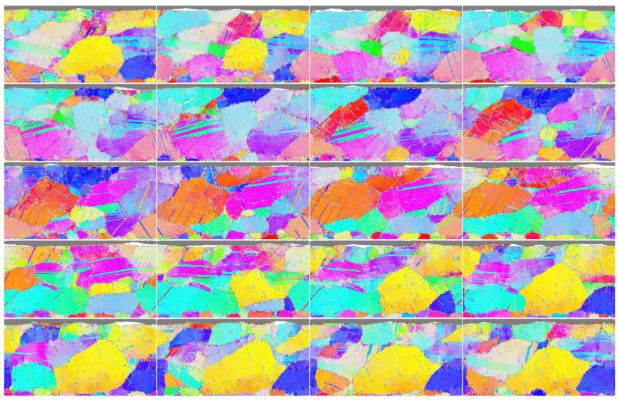

(f) $t = 7$ ns (forward)

Figure 2: Substrate tomographs of a rigid Fe counterbody sliding over a polycrystalline fcc Cu base body at 0.4 GPa normal pressure. Grains are colored according to orientation (inverse pole figure (IPF) standard, see legend in panel (b)), Fe counterbody is gray. Snapshots are shown after 0 ns (a), 3 ns (c), 5 ns (d), and 7 ns (f) of sliding in the positive x direction (to the right) as well as after sliding in positive x-direction for 5 ns, followed by sliding in the negative x direction for another 2 ns (e). Thus, (d) marks the turning point, while the other images are arranged so that (e) may be most easily compared to (a), (c), and (f).

previously effected intragranular lattice rotations and formed sub-grains is in agreement with experimental observations reported for bulk metals.[16] Concerning crystallographic texture, no clear trends can be extracted from our MD simulations due to the small number of grains, where the only plastically deformed ones are located in the immediate surface vicinity. There is little experimental data on the type of developed texture, and the majority of it refers to fcc metals. Some authors experimentally observed a $\{110\}\langle 211\rangle$ rolling texture on Cu, which corresponds to a pure shear system, whereas other authors have a torsion texture indicating simple shear, as summarized in 53.

The degree of plastic deformation undergone by the substrate during sliding is quantified based on the number of defects induced. Defects are formed by atoms not ordered according to a fcc structure, which are found at grain boundaries, dislocations, or at the surface. In our simulations, Cu undergoes twinning as the most prominent mode of deformation to accumulate plastic strain. This may be a result of the high strain rates due to the chosen sliding velocity of 80 m/s, but is in qualitative agreement with common deformation mechanisms in fcc lattices. Close-up visualizations reveal other defects such as single stacking faults, but these do not dominate in the current calculations. Thus, the atoms identified by the common neighbor analysis as twin boundaries, as a main defect class, are counted separately. The results are shown as the time dependent percentage of grain and twin boundary atoms, and are shown in Figs. 3a and b, respectively. The solid lines indicate unidirectional sliding, and these are the only lines plotted until 5 ns. Afterwards, additional dashed lines indicate the fraction of defects upon reversing the sliding direction. The fractions of GB atoms show that for the smallest contact pressure of 0.1 GPa, both lines are fairly time independent and overlap, indicating that the imparted strains are too low to induce a significant degree of deformation. An analogous result is achieved when increasing the contact pressure to 0.2 GPa. However, at 0.3 GPa contact pressure, the results show a clear divergence between both curves. The one obtained from a monotonic sliding direction rapidly increases after 5 ns, whereas the one obtained after a strain path reversal remains fairly constant. This behavior is much more pronounced at 0.4 GPa, where a reversal in the sliding direction results in an obvious reduction of the percentage of GB atoms. For the maximum contact pressure of 0.5 GPa, this behavior disappears, and a reversal in sliding direction does not result in a lower or steady density of defects. Consequently, the fraction of GB atoms confirms the qualitative information provided by the snapshots that for loads up to 0.4 GPa a recovery of the microstructure occurs upon reversing the sliding direction. In order to exclude any potential artifact caused by surface atoms, the plot in Fig. 3b shows the percentage of twin boundaries. These defects are exclusively caused by plasticity and provide a confirmation of the results previously shown in Fig. 3a. Again, a decrease in the fraction of twin boundary defects can be observed at contact pressures between 0.3 and 0.4 GPa. Lower normal pressures lead to smaller amounts of generated defects in the crystallographic structure, whereas the highest considered contact pressures result in similar behavior for the backward and forward sliding direction. Normal pressures exceeding 0.4 GPa lead to deformations of the entire substrate down to the lower model boundary, therefore some large grains may not behave as they would in a real system, which would mark the limit of applicability of the MD model in its current size.

So far, the obtained results show that a reversal of the sliding direction results in a recovery of the microstructure as a consequence

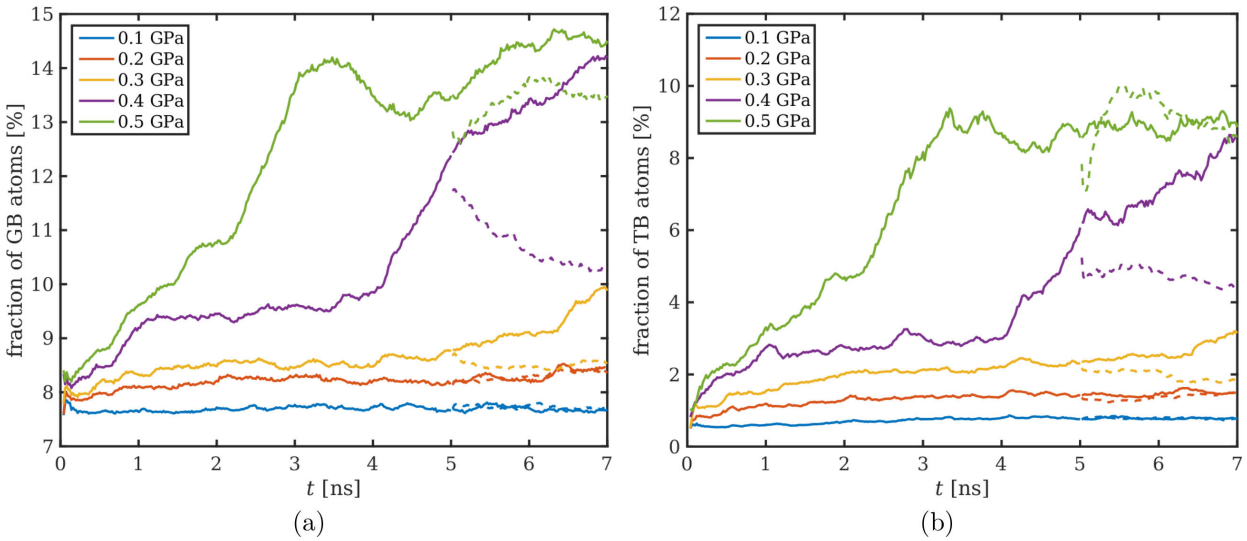

Figure 3: fcc Cu substrate. Fraction of grain boundaries (GB), dislocations and surface atoms (a) and twin boundary (TB) atoms (b) according to a common neighbor analysis (CNA) at five applied pressures. Dashed curves represent reverse sliding direction.

of the strain path change. With the aim of visualizing grain refinement and coarsening within the microstructure, we constructed a time series of histograms, formatted as a heat map of the grain diameter as a function of depth and time, see Fig. 4. For this, the measured quantity (grain boundary fraction) was converted into a typical grain diameter assuming the validity of the relationship between the two, shown in the insert in the top left of the figure. The heat maps indicate that even for a moderate contact pressure of 0.2 GPa, the grain size decreases in magnitude and depth as a function of time during the initial 5 ns of unidirectional sliding (Fig. 4a). Afterwards, the trend proceeds when maintaining the sliding direction for an additional 2 ns. By contrast, a reversal of the sliding direction results in a slight increase of the grain size below a depth of approximately 7 nm ($z = 33$ nm), but in further grain refinement within the near-surface region above. While the total defect fraction increase imparted by this contact pressure is rather small, reaching typical values of only 1–2 %, the highly non-linear relationship shown in the insert in Fig. 4 results in grain refinement down to half of the initial size in the near-surface region. For a contact pressure of 0.3 GPa, the observations are similar, but a marked difference arises upon reversal. In this case, a reversal in sliding direction results in a significant reduction of the defect fraction, in particular below 10 nm depth ($z = 30$ nm), where the substrate almost fully recovers to its initial defect fraction (Fig. 4b). This behavior becomes exacerbated at 0.4 GPa. Here, proceeding with unidirectional sliding beyond 5 ns results in drastic grain refinement permeating the entire depth of the polycrystalline substrate down to the fine-grained bottom layer, which is constrained due to the imposed boundary conditions. On the other hand, reversing the sliding direction results in a marked recovery of the substrate with grain coarsening occurring throughout the visualized range of the depth profile (Fig. 4c).

The development of the twin boundary (TB) atom densities is shown for the same loads in Fig. 5. Note that the histograms of the TBs are generally clearer than the respec-

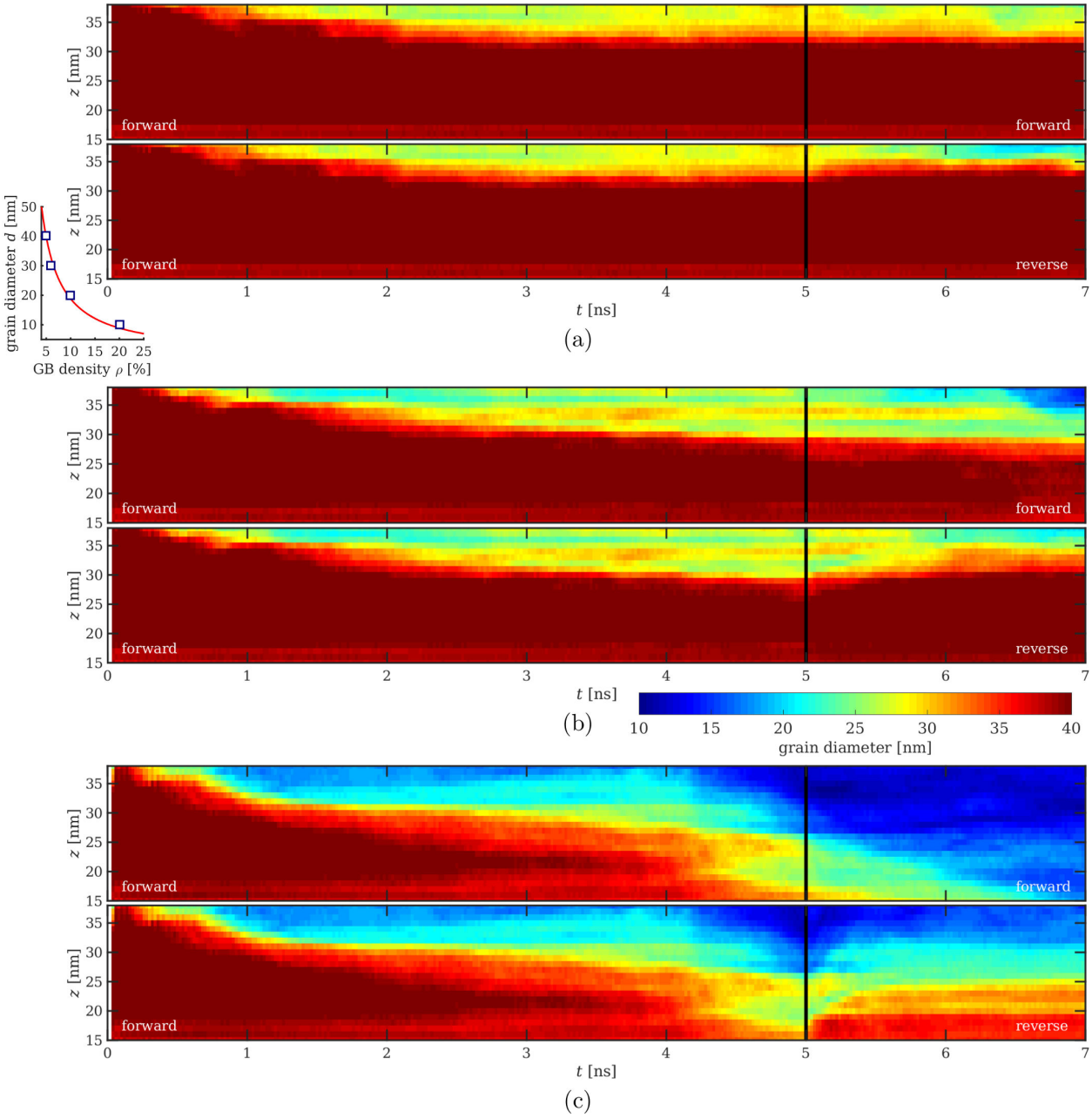

Figure 4: fcc Cu substrate. Depth profile of the mean grain diameter over time for three loads: 0.2 GPa (a), 0.3 GPa (b), and 0.4 GPa (c), assuming the relationship between GB fraction ρ and grain diameter d for (nano)crystalline fcc Cu shown in the insert (adapted from 10, with some of our own data and a rational-function fit $d = 226\,\rho^{-1.08}$). For each load, the top panel shows the results for 7 ns of unidirectional sliding, while the lower panel visualizes the results for 5 ns sliding in positive x direction and subsequent sliding in the opposite direction (sliding direction turning point marked by a thick black line). The substrate surface is located at $z = 40$ nm, and the lower 15 nm were omitted because they are dominated by the smaller grains in this region.

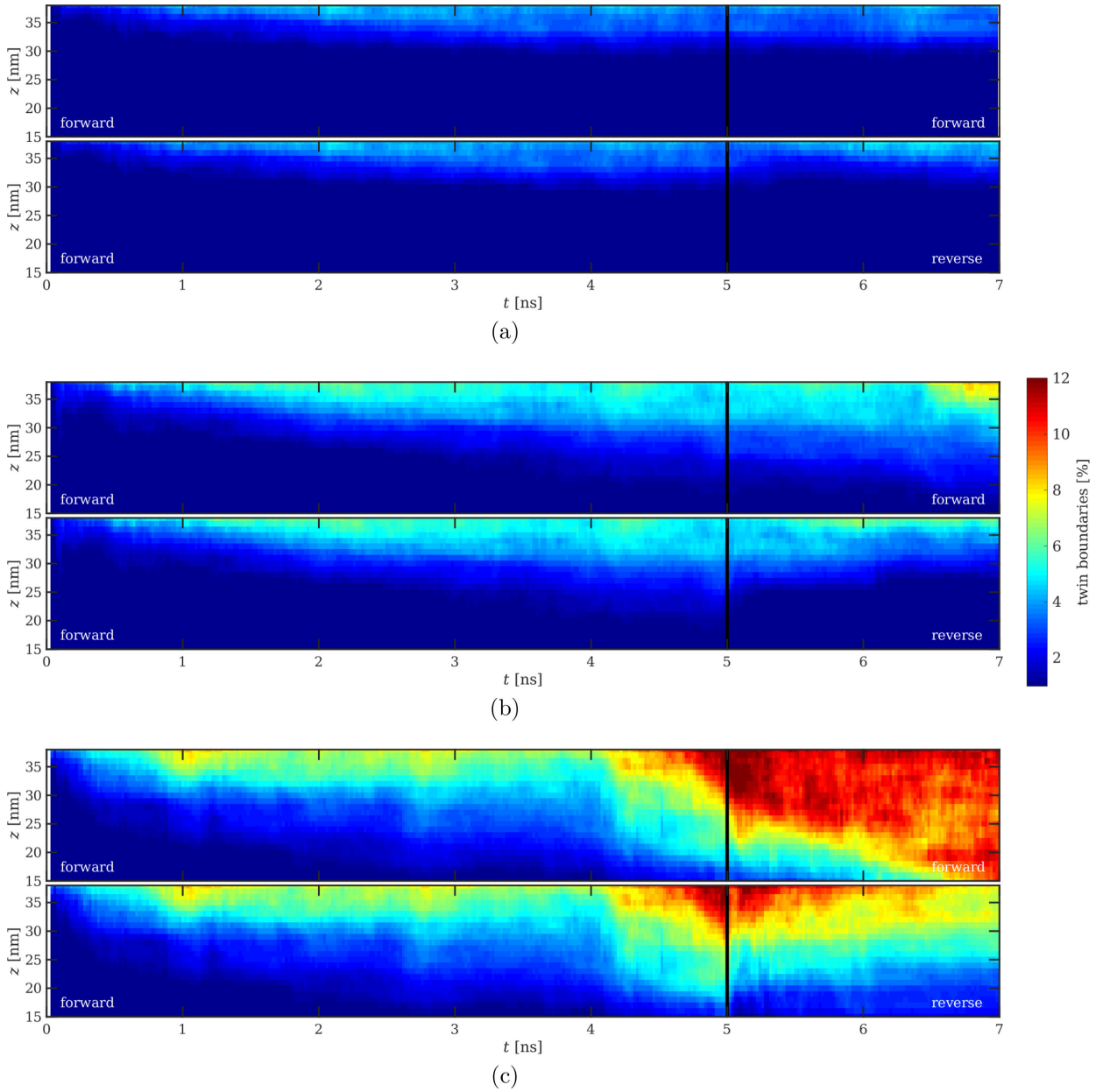

Figure 5: fcc Cu substrate. Depth profile of the twin boundaries over time for three loads: 0.2 GPa (a), 0.3 GPa (b), and 0.4 GPa (c). Similar presentation style to Fig. 4 with an intuitively inverted color scheme.

tive grain boundary analyses, as TB atoms are unambiguously identified as hcp structure by the common neighbor analysis. The color scheme is intuitively inverted with respect to Fig. 4 due to the inverse relationship between grain size and GB fraction. That said, similar trends to those discussed above can be observed in Fig. 5.

In what follows, the mechanisms that lead to a recovery of the microstructure are analyzed in higher detail by addressing the deformation and rotation of three selected spatial regions (Fig. 6). The first tracked region (top row) is a large grain of approximately 40 nm diameter and an initial lattice orientation [112]. After sliding for 3 ns, the imparted deformation leads to the formation of [122] twins and lattice rotations, reducing the initial grain size, whereas the lower part of the grain remains undeformed. After 5 ns, the smaller grains on the left side beneath the surface recrystallize to form a twinned grain, and the lattice of the previously formed subgrain on the right side rotates further towards the [122] twinning direction. At this point, when proceeding for an additional 2 ns in the original sliding direction, the grain basically splits into several sub-grains featuring a considerable number of intragranular rotations and defects. By contrast, reversing the sliding direction for 2 ns results in a recovery of most of the twins, which flip back to their original crystallographic direction. The grain is enlarged on the left by phagocytizing the neighboring grain. The final outcome of the strain path change is that the grain has a crystallographic orientation very close to the original [112], with the presence of some residual higher-index intragranular regions and [122] twins found in the upper region of the grain.

The center row focuses on four small grains of approximately 15 to 20 nm grain diameter. With increasing deformation, the light yellow grain rotates from [136] towards the [115] direction, whereas the grain below, initially oriented in [112], undergoes twinning at the top. The red grain, initially oriented in [100], remains in this orientation for the first 3 ns, in a similar way as the yellow [159] grain below it. After 5 ns, the imparted deformation results in significant changes in grain texture and morphology, and the presence of large intragranular lattice rotations results in a blurry point-cloud in the pole figure for each grain. If we maintain the sliding direction up to 7 ns, the situation becomes more dramatic. However, reversing the sliding direction results in a partial microstructural recovery. The four initial grains re-consolidate, and despite the presence of a small degree of intragranular lattice rotations, the IPF indicates only a small amount of orientation scatter within a given grain. One remarkable change when compared to the initial microstructure is that the light yellow [136] grain has split in two, with the upper section now oriented in [111] direction, while the lower section has merged with the neighboring grain oriented in [100]. The grain initially oriented in [112] has fully recovered its initial lattice orientation except for a minor twinned section, which lies outside the analyzed box and is consequently not represented in the IPF.

A similar recovery of the microstructure can be observed in the (red) grain shown in the bottom row of Fig. 6. The initial lattice orientation close to [100] is maintained after 3 ns, but proceeding with sliding results in massive sub-graining beneath the surface and formation of a high number of partial dislocations, some of them bent, and a rotation of the lower section of the grain to the [012] orientation after 7 ns. However, if we reverse the sliding direction after 5 ns, the resulting grain almost perfectly recovers its original shape with a perfect [100] orientation, albeit with a considerable density of partial dislocations. A detailed analysis of the defect evolution during sliding reversal is

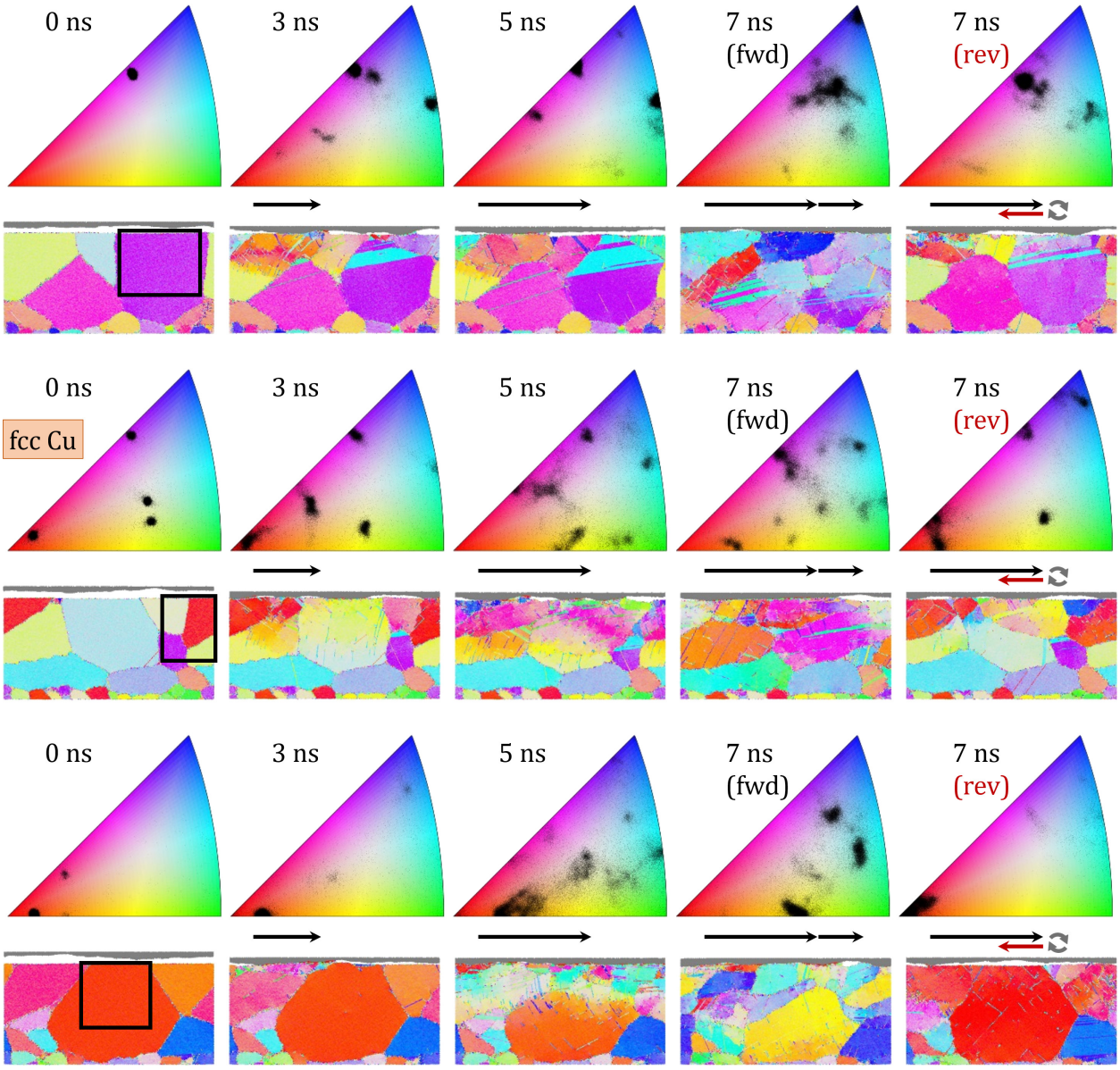

Figure 6: fcc Cu substrate, 0.4 GPa. Orientation maps (OM) of three (groups of) grains at five noteworthy points in time, with the corresponding cross-section of the sample directly underneath, coloring corresponds to that in Fig. 2. Every column represents a different time (0 ns, 3 ns, 5 ns, 7 ns, 7 ns with strain reversal), and the regions for which the OMs were produced are marked in the substrate tomographs in column 1.

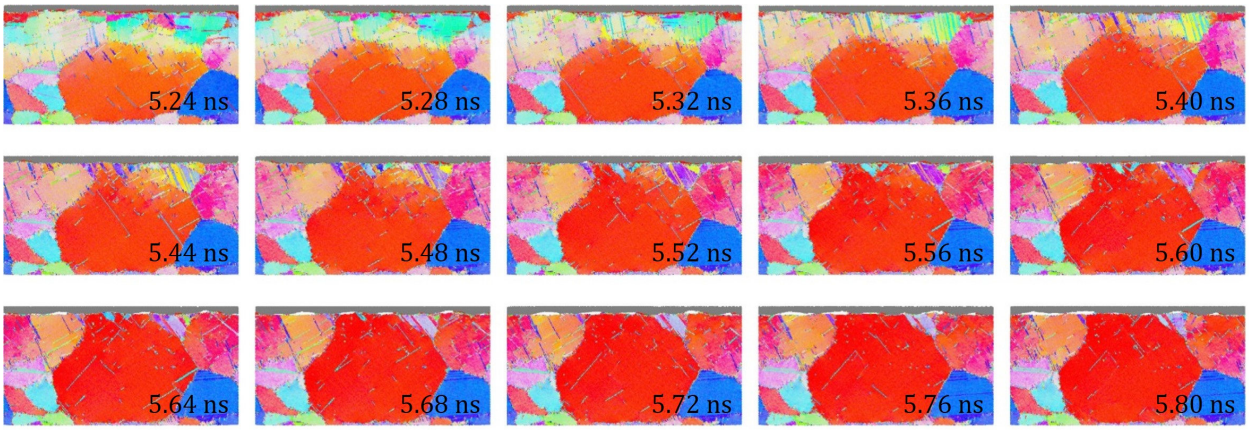

Figure 7: fcc Cu substrate, 0.4 GPa. Detail snapshots of grain number 3 after strain reversal. Frames are evenly distributed over a time span of approximately 0.6 ns. Coloring corresponds to that in Fig. 2.

shown in Fig. 7. The grain starts its recovery with the near-surface area split up into small grains. Upon sliding reversal, the dislocations move in such a way that the upper part of the grain starts recovering and growing at the expense of the previously formed surface grains. At $t = 5.52$ ns it can be observed that a small volume right beneath the surface progressively rotates towards the [100] direction. Initially, the density of intragranular dislocations seems to decrease, but from $t = 5.52$ ns on, no clear reduction of their density can be observed.

3.2 Microstructure evolution in a bcc Fe lattice

We ran an almost identical set of MD simulations using a polycrystalline substrate with the same grain morphology and crystallographic texture as the one previously used for copper. The only differences were that the interatomic potential was changed to represent Fe, the fcc crystal structure was replaced with a bcc one, and the loads were increased to be able to observe phenomena associated with the yield stress, which is approximately three times higher for iron than for copper.[54] The tomographic snapshots of the simulation run at a contact pressure of 1.2 GPa are shown in Fig. 8. During the initial sliding steps, the deformation imparted by the counterbody results mostly in the formation of intragranular lattice rotations with a certain degree of sub-graining visible after 5 ns. If we proceed with unidirectional sliding, we observe grain refinement in the immediate surface vicinity as well as grain rotation, e.g., a [123] oriented grain rotating towards the (green) [011] orientation (see Fig. 8f). Reversing the sliding direction results in an almost complete dissolution of the formed intragranular orientation mismatches, resulting in a massive recovery of the microstructure. The main mode of accumulating strain is visible as defect points, which are intersections of dislocation lines with the yz plane. Twins are not formed, though some of the dislocations could be identified as stacking faults.

The fraction of GB atoms as function of contact pressure shows that for contact pressures up to 0.9 GPa, there is not a significant difference between maintaining or reversing the sliding direction, see Fig. **??**. At the contact pressure of 1.2 GPa, the situation changes significantly. The fraction of GB

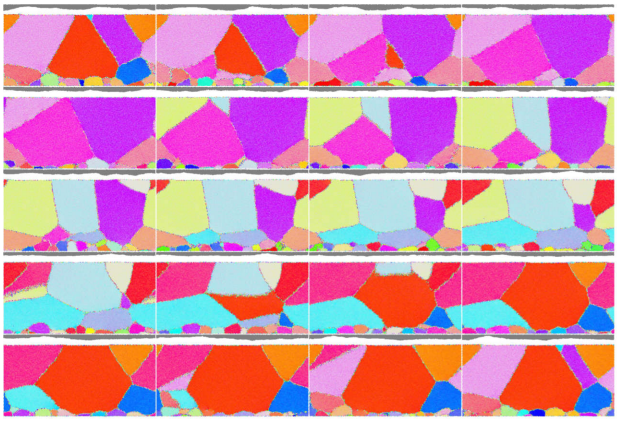

(a) $t = 0$ ns

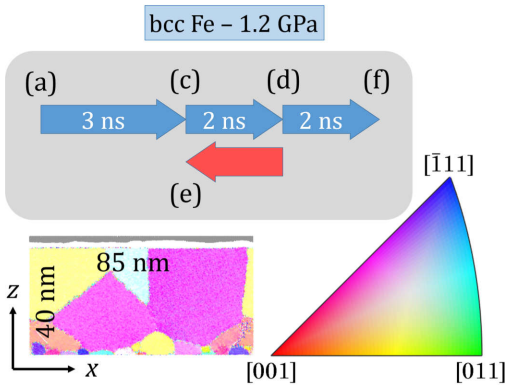

(b)

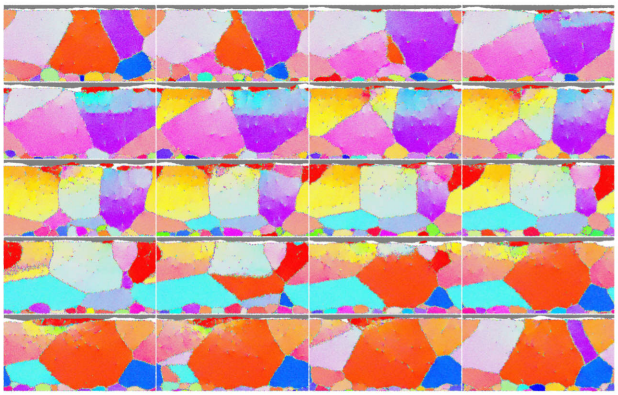

(c) $t = 3$ ns

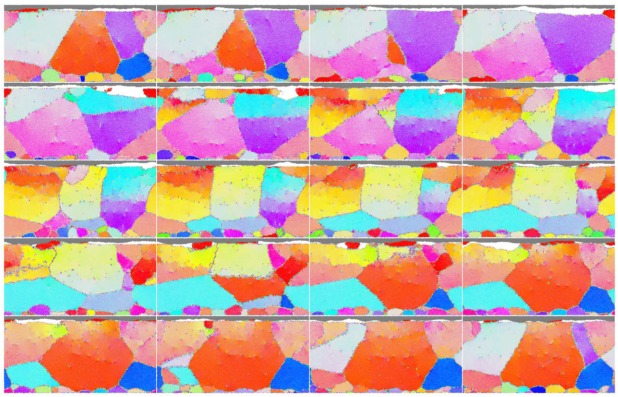

(d) $t = 5$ ns (turning point)

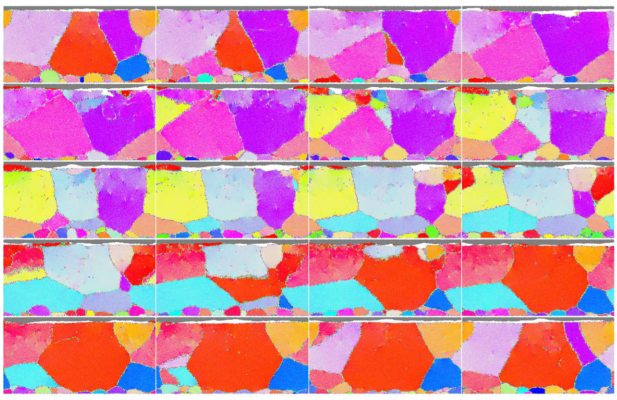

(e) $t = 7$ ns (reverse)

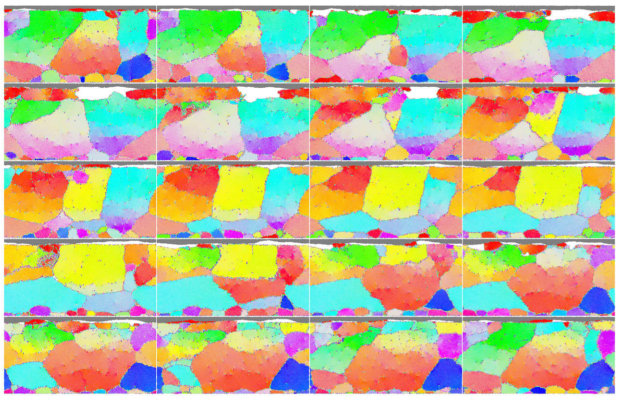

(f) $t = 7$ ns (forward)

Figure 8: Substrate tomographs of a rigid Fe counterbody sliding over a polycrystalline bcc Fe base body at 1.2 GPa normal pressure. Grains are colored according to orientation (inverse pole figure (IPF) standard, see legend in panel (b)), Fe counterbody is gray. Snapshots are shown after 0 ns (a), 3 ns (c), 5 ns (d), and 7 ns (f) of sliding in the positive x direction (to the right) as well as after sliding in positive x-direction for 5 ns, followed by sliding in the negative x direction for another 2 ns (e). Thus, (d) marks the turning point, while the other images are arranged so that (e) may be most easily compared to (a), (c), and (f).

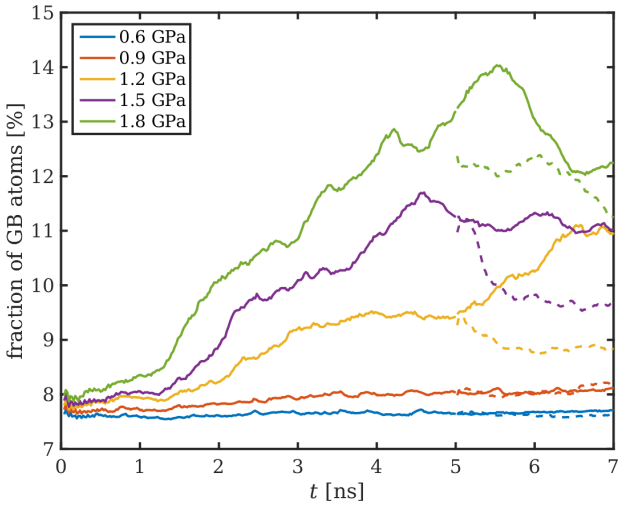

Figure 9: bcc Fe substrate. Fraction of grain boundaries (GB), dislocations and surface atoms according to a common neighbor analysis (CNA) at five applied pressures. Dashed curves represent reverse sliding direction.

atoms initially rises, as the imparted sliding time increases. After 5 ns, maintaining the sliding direction results in a further increase of the fraction of GB atoms. By contrast, reversing the sliding direction results in a reduction of the fraction of GB atoms by approximately 1 %. The trend observed when exerting a contact pressure of 1.5 GPa is analogous. However, imparting a higher pressure ($\sigma_z = 1.8$ GPa) results in similar behavior for forward and backward sliding, with the recovery of the microstructure being negligible. The reason for this effect is that comparatively large volumes of wear particles (visible as red [100] grains in the sliding interface) are formed that at times exert even higher local pressures and eventually recrystallize onto the surface.

The distribution of GB atoms and dislocations, which cannot be distinguished using CNA, is shown in Fig. 10 as a function of depth and time for three contact pressures. Note that for bcc Fe, a conversion to grain diameters similar to Fig. 4 is not meaningful, as the quantity measured using the common neighbor analysis is dominated by the defect fraction, which says only little about the grain size. The top heat map (Fig. 10a) shows an increase in defect fraction beneath the surface as time progresses. Proceeding with unidirectional sliding beyond 5 ns results in a further increase of the defect fraction, while a reversal of the sliding direction results in a visible reduction. A similar outcome is obtained for an increased contact pressure of 1.5 GPa (Fig. 10b). Here, the fraction of defects rises due to the increased contact pressure, and the affected depth is greater than for 1.2 GPa, but reversing the sliding direction results in a reduction of the total defect fraction, with a noticeable recovery within the deeper regions of the substrate. At the highest considered contact pressure of 1.8 GPa, the affected substrate region now covers most of the depth shown in Fig. 10c, but reversing the sliding direction no longer results in the overall recovery of the microstructure observed at lower loads. Although the total fraction of GBs remains approximately the same after the reversal, see the green curve in Fig. **??**, the generally observed recovery of the substrate at greater depths ($z < 30$ nm), where the number of

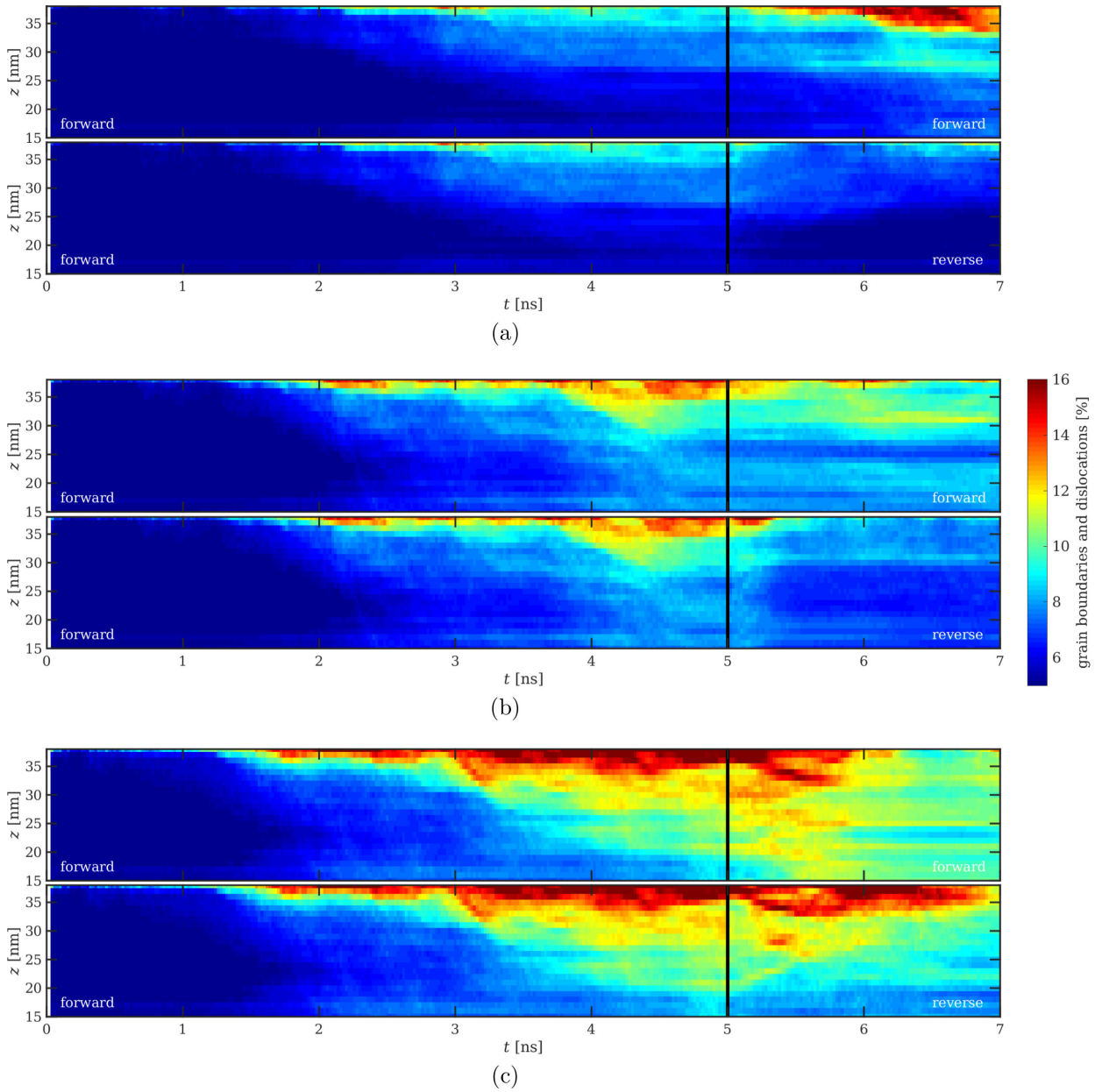

Figure 10: bcc Fe substrate. Depth profile of the grain boundary and dislocation fraction over time for three loads: 1.2 GPa (a), 1.5 GPa (b), and 1.8 GPa (c). Same presentation style as in Fig. 5.

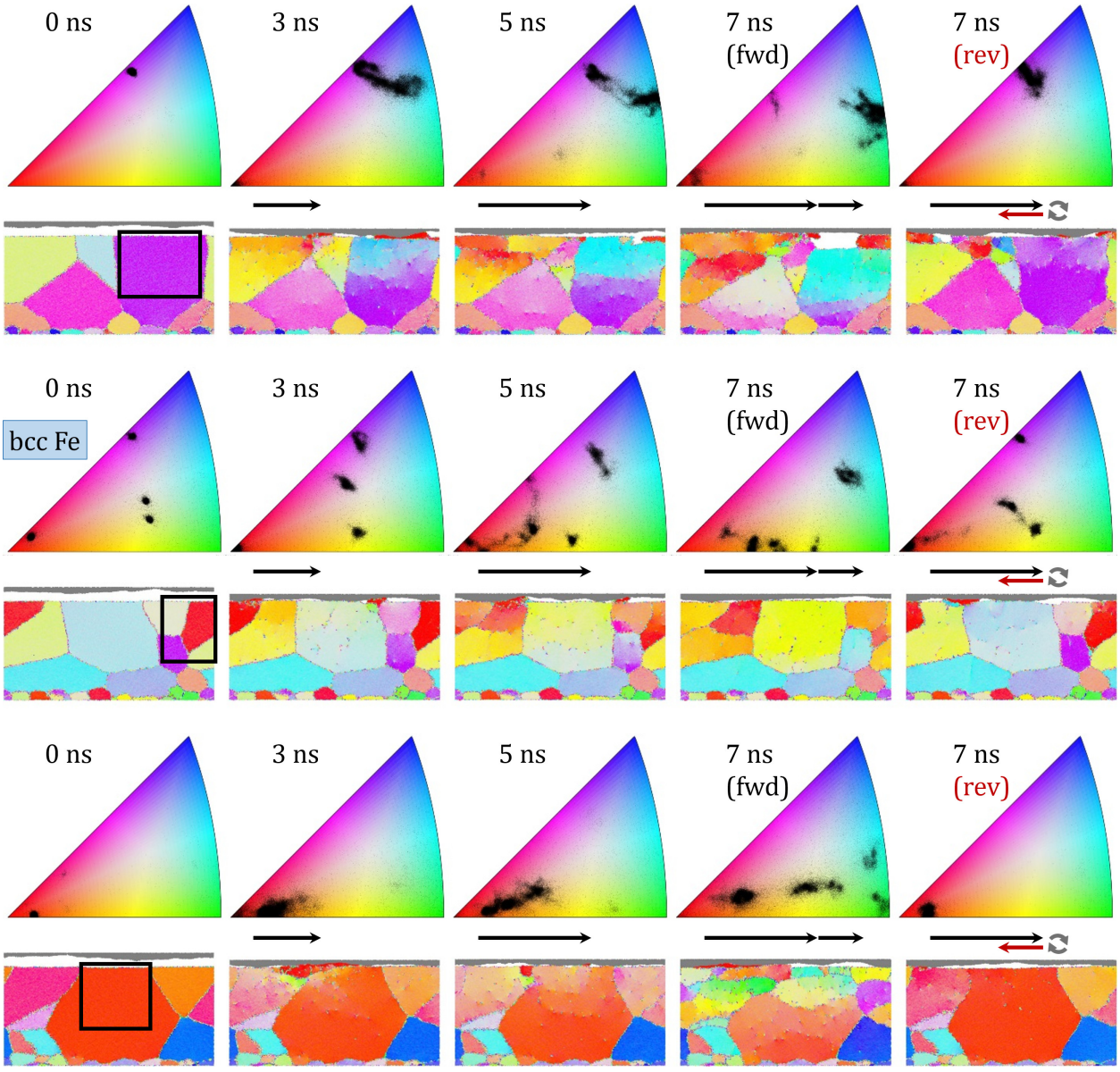

Figure 11: bcc Fe substrate, 1.2 GPa. Orientation maps (OM) of three (groups of) grains at five noteworthy points in time, with the corresponding cross-section of the sample directly underneath, same layout as Fig. 6.

generated dislocations is always smaller, is evident here as well.

A detailed analysis of the microstructure recovery upon strain path change is performed by following the lattice orientation and grain morphology of the same grains that were already analyzed in the Cu sample. The deformation was caused by the sliding counterbody at a contact pressure of 1.2 GPa. The first tracked grain is indicated by a black box in the upper row of Fig. 11. As in the Cu case, it has an initial diameter of 40 nm and an initial lattice orientation in the [112] direction. After 3 ns of sliding, the top half of the grain starts rotating towards the [122] direction. Both the top and the bottom part are characterized by the formation of intragranular misorientations, as indicated in the IPF by a blurry cloud of orientations spanning the region between [112] and [234] in the orientation map. The grain also contains a large number of dislocations as a consequence of the imparted plastic strain. After 5 ns, the grain has split into two grains, with the upper part having a consolidated [122] orientation and the lower part still featuring a high degree of intragranular mismatch. When proceeding with sliding in the same direction until 7 ns, almost the entire grain has a well-established [133] orientation, and only the very bottom part maintains the original orientation due to boundary constraints. However, if we reverse the sliding direction after 5 ns, the grain almost completely recovers its original [112] orientation, featuring only some degree of intragranular partial lattice rotations in the upper region.

A similar trend can be observed when tracking a group of smaller grains (center row of Fig. 11). In this case, the four grains have distinct initial lattice orientations, as shown in the IPF. After 3 ns, the grain oriented in [124] starts rotating while the remaining grains maintain their initial lattice orientations. With increasing sliding time, all four grains rotate, with one of the surface grains growing at the expense of its neighbor while rotating via [129] towards [015]. When reversing the sliding direction after 5 ns, all four grains rotate back to almost their exact initial orientations. This may be observed in the orientation map, where a low defect density is indicated by the low amount of scatter in the four clusters.

The third illustrative example also highlights the recovery of the microstructure upon strain reversal. In this case, the red [100] grain of 50 nm keeps on refining into smaller grains oriented in [129], [159], [157], and [133] if we maintain the sliding direction up to 7 ns. This might partially be attributed to welding effects of wear particles caught in the sliding interface, and thus locally much higher pressures. However, when reversing the sliding direction, the grain reverts perfectly to its initial orientation, only featuring a higher level of defects as indicated by the blurriness of the cluster in the orientation map (bottom row of Fig. 11).

Figure 12 shows a detailed time sequence of snapshots illustrating the microstructure recovery of the tomographic section illustrated in the top row of Fig. 11 upon sliding reversal. First, the dislocations are aligned parallel to the surface and seem to form a sub-cell in the top left, growing until 5.6 ns, at which time the emitted dislocations are arranged at the cell boundary. During this period, we also observe that a topographic wear scar on the surface (top right of the section) heals via asperity interaction. At 6.08 ns, the cell begins rotating back towards the initial [112] orientation of the bottom part of the grain, even though a larger dislocation density is still visible at the interface between the cell and the lower grain. Afterwards, the former cell starts growing towards the left until at the end of the process (6.4 ns), most of the two grains present at the point of reversal are merged into a single lattice orienta-

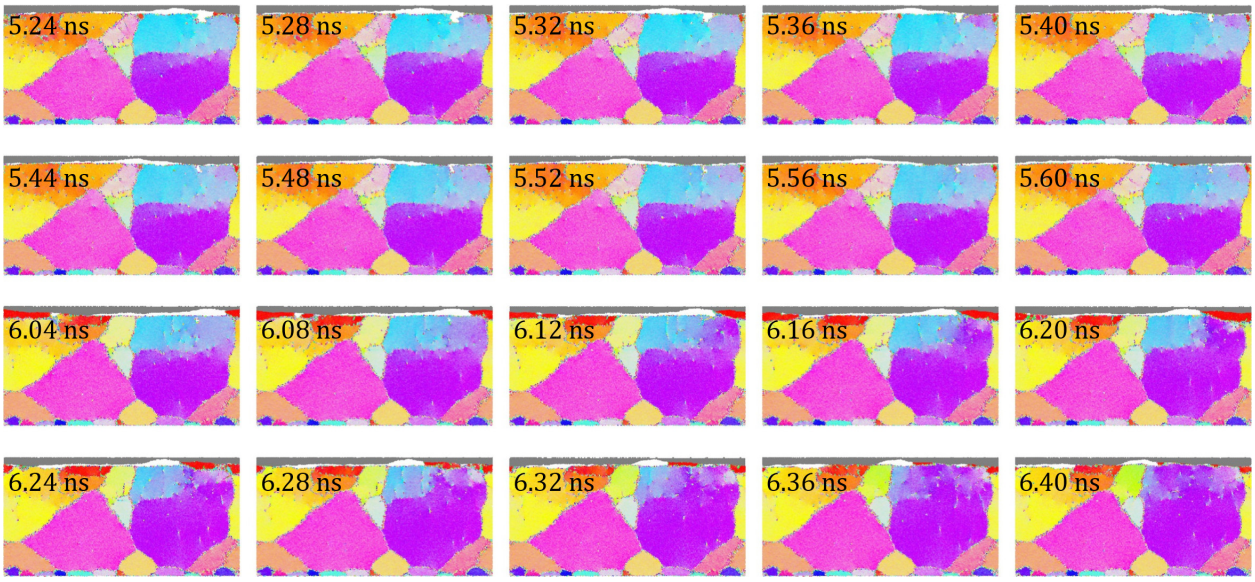

Figure 12: bcc Fe substrate, 1.2 GPa. Detail snapshots of grain number 1 after strain reversal. Rows 1 and 2: Removal of a wear scar via asperity interaction over a time span of 0.4 ns. Rows 3 and 4: Rotation of cyan-colored sub-grain into its original orientation over a time span of 0.4 ns.

tion, even though the upper part still features a large number of dislocations, whereas the lower part remains virtually defect-free. A movie of the sliding process in reverse direction reveals that the dislocations in the lower part of the grain are constantly moving upwards towards the surface.

4 Discussion

The obtained results reveal a load-dependent recovery of the near-surface microstructure when reversing the sliding direction. The recovery of microstructure upon strain reversal has been long known in bulk metals, but it had not yet been proved that such microstructural behavior occurred at the interface between counterbodies in relative sliding motion. The only work suggesting that such behavior occurs at the sliding interface was by Rodríguez Ripoll *et al.*,[35] who experimentally observed it indirectly as a transient softening upon strain reversal. This transient softening stage caused by microstructural recovery upon strain path changes could be successfully captured by Kitayama *et al.*[55] using an extended RGBV model, named after the authors of 56. The RGBV model explicitly accounts for the accumulation and annihilation of dislocations during strain path changes by dividing the dislocation density during strain hardening into two populations called forward and reverse dislocations. During monotonic loading both populations rise, but upon strain reversal only the reverse dislocations are allowed to recombine. The fraction of reversible dislocations is a function of strain, being initially zero. By using this modeling approach, a change in loading direction leads to a transient softening stage, as observed experimentally due to the accumulation and annihilation of dislocations during this stage.

The MD simulation of polycrystalline and random substrates with fcc or bcc lattices could reflect experimentally observed effects in sliding contact surfaces. The main mode

to accumulate plastic strain in bcc lattices showed to be stacking faults and formation of new grains directly beneath the surface by local lattice rotation. For fcc lattices the main defects forming were twins along with grain formation like in bcc. Upon strain path reversal all these defects were reduced in number and depth from the surface. The extent of these changes were directly, but not linearly, linked to the exerted initial contact pressures. A profound understanding of sub-surface damage evolution in sliding contacts is essential for understanding the surface degradation mechanisms that ultimately lead to wear. In bulk materials, strain reversals also play a crucial role in fatigue,[57] since damage accumulation leading to crack initiation and propagation is also caused by dislocation networks evolving upon strain reversal. The dissolution of dislocation pile-ups upon strain reversal has been recently experimentally observed on copper micro-cantilevers[58] in the context of low cycle fatigue. There, *in situ* Laue diffraction measurements after bending revealed the formation of geometrically necessary dislocation arrangements that disappear upon unloading. This dissolution of dislocation pile-ups and/or dislocation cells during reverse loading leads to the macroscopically observed offset in the yield stress upon load reversal.

The most significant microstructural recovery occurs for the intermediate contact pressures considered in our simulations. For Cu, contact pressures up to 0.3 GPa lead to small imparted strains in the metal's near-surface region, so that the annihilation process is negligible. In this case, the grains located directly beneath the contact interface adapt immediately to the new strain direction by developing a new microstructure, as the dislocation density generated before the strain path change is low. At intermediate contact pressures, the annihilation of dislocations and the re-orientation of the individual sub-grains towards their initial orientation is higher due to the formation of a well-established microstructure in the initial strain direction. Using MD simulations, Yue *et al.* also found a lower defect density in copper subject to reciprocating sliding contact than for unidirectional loading.[59] In their case, the number of sliding passes was limited to two (same direction and reciprocating). The copper substrate was selected to represent single crystalline copper and a bi-crystal with either a twinned boundary (sigma 3) or a twist boundary (sigma 7). For the two former substrates, the number of defects was smaller after bidirectional sliding, compared to two passes in the same direction. By contrast, the bi-crystal substrate with the twist grain boundary exhibited the opposite behavior, which indicates that twinned boundaries are less prone to defect accumulation under reciprocating sliding. Indeed in our MD simulations performed on copper, the snapshots reveal that many twins recover the original lattice orientation after reversing the sliding direction. However, in our system the fraction of grain boundary atoms that disappear upon sliding direction reversal is even more pronounced when compared to the fraction of twin boundary atoms. With increasing imparted pre-deformation, the severity of the transient softening stage becomes more dramatic, as shown experimentally .[16] However, in our MD studies, the highest applied contact pressures led to microstructures that do not revert to configurations similar to the initial ones upon reversing the sliding direction. There seems to be a critical contact pressure above which the reversibility of the microstructure stops. So far, there does not seem to be a convincing explanation to justify this behavior that seems to be exclusive of metal interfaces. One possibility would be that a numerical boundary effect arises at large contact pressures, i.e., deformation occurs at such great depths that the finite

size of the modeled polycrystalline substrate starts impeding some of the mechanisms that would occur in real systems. A second possibility would be that the irreversibility of the microstructure arises from the generation of wear particles during the sliding process and the presence of an interface, followed by recrystallization of these particles onto the substrate. The combination of both effects can lead to the formation of vortices at the interface between the two sliding counterbodies. Kim *et al.*[60] studied the behavior of crystalline materials engaging in sliding contact for self-mated, similar, and hard–soft contact pairs.[60] In their work, the authors observed vorticity development, leading to the presence of eddies in the immediate vicinity of the siding interface. These vortices were attributed to Kelvin-Helmholtz instabilities, in an analogy to turbulent flow in fluids. Similar observations had been previously made for amorphous materials. An MD study carried out using a Fe–Cu system even indicated that the formation of nanocrystalline grains may also be influenced by vorticity-driven dynamic recrystallization.[61] This vorticity effect was later attributed to bulge formation on grains with suitably oriented slip systems, a process which differs substantially from Kelvin-Helmholtz instabilities in fluids.[62] That said, the formation of vortices was recently experimentally observed in a multilayer Cu/Au system under reciprocating sliding using a nanoindenter.[63]

The simulations performed in this work show an initial peak of the coefficient of friction upon strain reversal at medium to high normal pressures, followed by a decrease well below the level occurring in unidirectional sliding. At the highest considered pressures, no clear difference between unidirectional sliding and reversed sliding emerged. Therefore, as in 35, no conclusive assessment could be made regarding the evolution of friction during sliding reversal. The reason for this may lie in the complexity of the process, since beside the microstructural recovery that was clearly observed in both works, other factors can influence friction during the transient reversal, such as topographical changes or the presence of wear debris generated in the initial sliding direction. Therefore, there is still a clear need to address this issue in future works.

5 Conclusion

The polycrystalline MD approach presented in this work was used to monitor and identify microstructural changes that occur after reversing the sliding direction in a tribological contact. The results indicate a build-up of defect densities during the initial sliding phase and a clear reduction of the observed defects upon reversal. Thus, the applicability of polycrystalline MD simulation for reproducing well-known bulk phenomena arising from strain path changes, such as the Bauschinger effect, could be demonstrated using the example of a complex sliding process featuring a rough counterbody by studying the microstructural development in the near-surface region.

The influence of the lattice type was studied using fcc Cu and bcc Fe polycrystals as the main constituents of technologically relevant alloys such as steels, brass, or bronze, which are widely used in fundamental machine elements like gears or journal bearings. For both crystal lattices a hardening effect could be reproduced, as the dislocation density increased with depth for longer sliding times and higher normal pressures. With increasing sliding time, partial lattice rotation and alignment of dislocations could be observed in the substrate, followed by the formation of sub-grains beneath the surface. Upon strain reversal, most of these surface grains vanished and left behind only an in-

creased dislocation density compared to the initial structure, but nearly fully restored the previously observed grain morphologies. Thus, the microstructural changes that lead to significant hardening rate variations and even to a transient softening stage in bulk metals undergoing strain path changes were shown to occur in a sliding contact and could be monitored *in-situ* in a polycrystalline MD model at various external loads.

The spatial and temporal evolution of defects as well as differences between the two cubic lattices were quantified by grain- and twin boundary densities as well as defect histograms. For bcc Fe, sub-grain formation was followed by massive grain rotation that covers the entire substrate when the strain path remains unchanged. In contrast to that, the fcc Cu substrate is dominated by the formation of partial dislocations and twins (because of low stacking fault energy)—also within the newly formed sub-grains. Upon strain path reversal of the Cu substrate, the number of sub-grains and dislocations are reduced in number and depth.

The missing microstructural recovery upon sliding reversal beyond applied pressures of 0.4 GPa and 1.5 GPa for Cu and Fe, respectively, may either indicate the existence of a strain threshold beyond which the material cannot return to its pristine structure anymore, or it might represent a numerical size effect and thus the application limit of the MD model.

Acknowledgements

This work was funded by the Austrian COMET-Program (Project K2, XTribology, no. 849109) and carried out at the "Excellence Centre of Tribology". The government of Lower Austria is gratefully acknowledged for financially supporting the endowed professorship tribology at the Vienna University of Technology (Grant no. WST3-F-5031370/001-2017) in collaboration with AC2T research GmbH. The authors wish to thank Gerhard Betz and Simon Medina for reading through the manuscript and giving many valuable suggestions.

References

(1) Rigney, D.; Hirth, J. Plastic deformation and sliding friction of metals. *Wear* **1979**, *53*, 345–370.

(2) Rainforth, W.; Stevens, R.; Nutting, J. Deformation structures induced by sliding contact. *Philosophical Magazine A* **1992**, *66*, 621–641.

(3) Moshkovich, A.; Perfilyev, V.; Bendikov, T.; Lapsker, I.; Cohen, H.; Rapoport, L. Structural evolution in copper layers during sliding under different lubricant conditions. *Acta Materialia* **2010**, *58*, 4685–4692.

(4) Rigney, D. Transfer, mixing and associated chemical and mechanical processes during the sliding of ductile materials. *Wear* **2000**, *245*, 1–9.

(5) Rigney, D. A.; Karthikeyan, S. The evolution of tribomaterial during sliding: a brief introduction. *Tribology Letters* **2010**, *39*, 3–7.

(6) Greiner, C.; Liu, Z.; Strassberger, L.; Gumbsch, P. Sequence of stages in the microstructure evolution in copper under mild reciprocating tribological loading. *ACS applied materials & interfaces* **2016**, *8*, 15809–15819.

(7) Rupert, T. J.; Schuh, C. A. Sliding wear of nanocrystalline Ni–W: Structural evolution and the apparent breakdown of Archard scaling. *Acta Materialia* **2010**, *58*, 4137–4148.

(8) Li, W.; Tao, N.; Han, Z.; Lu, K. Comparisons of dry sliding tribological behaviors between coarse-grained and nanocrystalline copper. *Wear* **2012**, *274*, 306–312.

(9) Argibay, N.; Chandross, M.; Cheng, S.; Michael, J. R. Linking microstructural evolution and macro-scale friction behavior in metals. *Journal of Materials Science* **2017**, *52*, 2780–2799.

(10) Li, A.; Szlufarska, I. How grain size controls friction and wear in nanocrystalline metals. *Physical Review B* **2015**, *92*, 075418.

(11) Young Jr, J. L.; Kuhlmann-Wilsdorf, D.; Hull, R. The generation of mechanically mixed layers (MMLs) during sliding contact and the effects of lubricant thereon. *Wear* **2000**, *246*, 74–90.

(12) Wolff, K.; Liu, Z.; Braun, D.; Schneider, J.; Greiner, C. Chronology of the microstructure evolution for pearlitic steel under unidirectional tribological loading. *Tribology International* **2016**, *102*, 540–545.

(13) Stoyanov, P.; Merz, R.; Romero, P. A.; Wählisch, F. C.; Abad, O. T.; Gralla, R.; Stemmer, P.; Kopnarski, M.; Moseler, M.; Bennewitz, R.; Dienwiebel, M. Surface Softening in Metal–Ceramic Sliding Contacts: An Experimental and Numerical Investigation. *ACS Nano* **2015**, *9*, 1478–1491.

(14) Davenport, S.; Higginson, R. Strain path effects under hot working: an introduction. *Journal of Materials Processing Technology* **2000**, *98*, 267–291.

(15) Bauschinger, J. Über die Veränderungen der Elastizitätsgrenze und der Festigkeit des Eisens und Stahls durch Strecken, Quetschen, Erwärmen, Abkühlen und durch oftmals wiederholte Belastung. *Mitt: Mech-Tech Lab* **1886**, 1–116.

(16) Rauch, E.; Gracio, J.; Barlat, F. Work-hardening model for polycrystalline metals under strain reversal at large strains. *Acta Materialia* **2007**, *55*, 2939–2948.

(17) Lopes, A.; Barlat, F.; Gracio, J.; Duarte, J. F.; Rauch, E. Effect of texture and microstructure on strain hardening anisotropy for aluminum deformed in uniaxial tension and simple shear. *International Journal of Plasticity* **2003**, *19*, 1–22.

(18) Vincze, G.; Rauch, E.; Gracio, J.; Barlat, F.; Lopes, A. A comparison of the mechanical behaviour of an AA1050 and a low carbon steel deformed upon strain reversal. *Acta Materialia* **2005**, *53*, 1005–1013.

(19) Christodoulou, N.; Woo, O.; MacEwen, S. Effect of stress reversals on the work hardening behaviour of polycrystalline copper. *Acta Metallurgica* **1986**, *34*, 1553–1562.

(20) Yapici, G.; Beyerlein, I.; Karaman, I.; Tome, C. Tension–compression asymmetry in severely deformed pure copper. *Acta Materialia* **2007**, *55*, 4603–4613.

(21) Bartolomé, R.; Jorge-Badiola, D.; Astiazarán, J.; Gutiérrez, I. Flow stress behaviour, static recrystallisation and precipitation kinetics in a Nb-microalloyed steel after a strain reversal. *Materials Science and Engineering: A* **2003**, *344*, 340–347.

(22) Rauch, E.; Schmitt, J.-H. Dislocation substructures in mild steel deformed in simple shear. *Materials Science and Engineering: A* **1989**, *113*, 441–448.

(23) Yoshida, F.; Uemori, T.; Fujiwara, K. Elastic–plastic behavior of steel sheets under in-plane cyclic tension–compression at large strain. *International Journal of Plasticity* **2002**, *18*, 633–659.

(24) Sun, L.; Wagoner, R. Proportional and non-proportional hardening behavior of dual-phase steels. *International Journal of Plasticity* **2013**, *45*, 174–187.

(25) Christodoulou, N. Evolution of the Bauschinger effect in tension and compression in Zircaloy-2. *Acta Metallurgica* **1989**, *37*, 529–539.

(26) Knezevic, M.; Beyerlein, I. J.; Brown, D. W.; Sisneros, T. A.; Tomé, C. N. A polycrystal plasticity model for predicting mechanical response and texture evolution during strain-path changes: application to beryllium. *International Journal of Plasticity* **2013**, *49*, 185–198.

(27) Zecevic, M.; Knezevic, M.; Beyerlein, I. J.; Tomé, C. N. An elasto-plastic self-consistent model with hardening based on dislocation density, twinning and de-twinning: application to strain path changes in HCP metals. *Materials Science and Engineering: A* **2015**, *638*, 262–274.

(28) Ripoll, M. R.; Reisacher, E.; Riedel, H. Texture induced tension–compression asymmetry of drawn tungsten wires. *Computational Materials Science* **2009**, *45*, 788–792.

(29) Nesterova, E.; Bacroix, B.; Teodosiu, C. Experimental observation of microstructure evolution under strain-path changes in low-carbon IF steel. *Materials Science and Engineering: A* **2001**, *309*, 495–499.

(30) Wen, W.; Borodachenkova, M.; Tomé, C.; Vincze, G.; Rauch, E.; Barlat, F.; Grácio, J. Mechanical behavior of low carbon steel subjected to strain path changes: Experiments and modeling. *Acta Materialia* **2016**, *111*, 305–314.

(31) Tang, C.; Li, D.; Wen, G. Baushinger's Effect in Wear of Materials. *Tribology letters* **2011**, *41*, 569–572.

(32) Tang, C.; Wang, J.; Wen, G.; Wang, Y.; Li, D. Bauschinger effect in wear of Cu–40Zn alloy and its variations with the wear condition. *Wear* **2011**, *271*, 1237–1243.

(33) Tang, C.; Li, D.; Wen, G. A follow-up study on Bauschinger's effect in bidirectional wear of Cu-40% Zn against different types of counter-face. *Tribology Letters* **2011**, *43*, 101–106.

(34) Harea, E.; Lapsker, I.; Laikhtman, A.; Rapoport, L. Bauschinger's effect and dislocation structure under friction of LiF single crystals. *Tribology Letters* **2013**, *52*, 205–212.

(35) Ripoll, M. R.; Linz, M.; Gachot, C. Transient softening in lubricated sliding contacts due to strain path changes. *Wear* **2017**, *376*, 1728–1738.

(36) Eder, S. J.; Bianchi, D.; Cihak-Bayr, U.; Gkagkas, K. Methods for atomistic abrasion simulations of laterally periodic polycrystalline substrates with fractal surfaces. *Comput. Phys. Commun.* **2017**, *212*, 100–112.

(37) Eder, S. J.; Cihak-Bayr, U.; Bianchi, D.; Feldbauer, G.; Betz, G. Thermostat Influence on the Structural Development and Material Removal during Abrasion of Nanocrystalline Ferrite. *ACS Applied Materials & Interfaces* **2017**, *9*, 13713–13725.

(38) Plimpton, S. J. Fast parallel algorithms for short-range molecular dynamics. *J. Comput. Phys.* **1995**, *117*, 1–19.

(39) Bonny, G.; Pasianot, R. C.; Castin, N.; Malerba, L. Ternary Fe–Cu–Ni many-body potential to model reactor pressure vessel steels: first validation by simulated thermal annealing. *Philosophical magazine* **2009**, *89*, 3531–3546.

(40) Finnis, M. W.; Sinclair, J. E. A simple empirical N-body potential for transition metals. *Philosophical Magazine A* **1984**, *50*, 45–55.

(41) Mendelev, M. I.; Han, S.; Srolovitz, D. J.; Ackland, G. J.; Sun, D. Y.; Asta, M. Development of new interatomic potentials appropriate for crystalline and liquid iron. *Philosophical Magazine* **2003**, *83*, 3977–3994.

(42) Ashkenazy, Y.; Vo, N. Q.; Schwen, D.; Averback, R. S.; Bellon, P. Shear induced chemical mixing in heterogeneous systems. *Acta Materialia* **2012**, *60*, 984–993.

(43) Eder, S. J.; Cihak-Bayr, U.; Bianchi, D. Single-asperity contributions to multi-asperity wear simulated with molecular dynamics. *IOP Conference Series: Materials Science and Engineering* **2016**, *119*, 012009.

(44) Ewen, J. P.; Restrepo, S. E.; Morgan, N.; Dini, D. Nonequilibrium molecular dynamics simulations of stearic acid adsorbed on iron surfaces with nanoscale roughness. *Tribology International* **2017**, *107*, 264–273.

(45) Eder, S. J.; Cihak-Bayr, U.; Vernes, A.; Betz, G. Evolution of topography and material removal during nanoscale grinding. *Journal of Physics D: Applied Physics* **2015**, *48*, 465308.

(46) Larsen, P. M.; Schmidt, S.; Schiøtz, J. Robust structural identification via polyhedral template matching. *Modelling and Simulation in Materials Science and Engineering* **2016**, *24*, 055007.

(47) Stukowski, A. Visualization and analysis of atomistic simulation data with OVITO–the Open Visualization Tool. *Modelling and Simulation in Materials Science and Engineering* **2009**, *18*, 015012.

(48) Bachmann, F.; Hielscher, R.; Schaeben, H. Texture analysis with MTEX–free and open source software toolbox. Solid State Phenomena. 2010; pp 63–68.

(49) Nolze, G.; Hielscher, R. Orientations–perfectly colored. *Journal of Applied Crystallography* **2016**, *49*, 1786–1802.

(50) Faken, D.; Jónsson, H. Systematic analysis of local atomic structure combined with 3D computer graphics. *Computational Materials Science* **1994**, *2*, 279–286.

(51) Tsuzuki, H.; Branicio, P. S.; Rino, J. P. Structural characterization of deformed crystals by analysis of common atomic neighborhood. *Computer physics communications* **2007**, *177*, 518–523.

(52) Eder, S. J.; Cihak-Bayr, U.; Pauschitz, A. Nanotribological simulations of

multi-grit polishing and grinding. *Wear* **2015**, *340*, 25–30.

(53) Rainforth, W. Microstructural evolution at the worn surface: a comparison of metals and ceramics. *Wear* **2000**, *245*, 162–177.

(54) Howatson, A. M. *Engineering tables and data*; Springer Science & Business Media, 2012.

(55) Kitayama, K.; Tomé, C.; Rauch, E.; Gracio, J.; Barlat, F. A crystallographic dislocation model for describing hardening of polycrystals during strain path changes. Application to low carbon steels. *International Journal of Plasticity* **2013**, *46*, 54–69.

(56) Rauch, E.; Gracio, J.; Barlat, F.; Vincze, G. Modelling the plastic behaviour of metals under complex loading conditions. *Modelling and Simulation in Materials Science and Engineering* **2011**, *19*, 035009.

(57) Stricker, M.; Weygand, D.; Gumbsch, P. Irreversibility of dislocation motion under cyclic loading due to strain gradients. *Scripta Materialia* **2017**, *129*, 69–73.

(58) Kirchlechner, C.; Imrich, P. J.; Liegl, W.; Pörnbacher, J.; Micha, J.-S.; Ulrich, O.; Motz, C. On the reversibility of dislocation slip during small scale low cycle fatigue. *Acta Materialia* **2015**, *94*, 69–77.

(59) Yue, L.; Zhang, H.; Li, D. Defect generation in nano-twinned, nano-grained and single crystal Cu systems caused by wear: A molecular dynamics study. *Scripta Materialia* **2010**, *63*, 1116–1119.

(60) Kim, H.-J.; Karthikeyan, S.; Rigney, D. A simulation study of the mixing, atomic flow and velocity profiles of crystalline materials during sliding. *Wear* **2009**, *267*, 1130 – 1136, 17th International Conference on Wear of Materials.

(61) Karthikeyan, S.; Agrawal, A.; Rigney, D. Molecular dynamics simulations of sliding in an Fe–Cu tribopair system. *Wear* **2009**, *267*, 1166 – 1176, 17th International Conference on Wear of Materials.

(62) Beckmann, N.; Romero, P. A.; Linsler, D.; Dienwiebel, M.; Stolz, U.; Moseler, M.; Gumbsch, P. Origins of Folding Instabilities on Polycrystalline Metal Surfaces. *Phys. Rev. Applied* **2014**, *2*, 064004.

(63) Luo, Z.-P.; Zhang, G.-P.; Schwaiger, R. Microstructural vortex formation during cyclic sliding of Cu/Au multilayers. *Scripta Materialia* **2015**, *107*, 67–70.